Acta Cryst A FOUNDATIONS ADVANCES

ISSN 2053-2733

Bonding network and stability of clusters: the case study of $Al_{13}TM_4$ pseudo-tenfold surfaces

Philippe Scheid,[a,b] Corentin Chatelier,[b,c] Julian Ledieu,[b] Vincent Fournée[b] and Émilie Gaudry[b]*

[a]Mines Nancy, Université de Lorraine, Campus Artem, Nancy, France, [b]Université de Lorraine, CNRS UMR7198, Institut Jean Lamour, F-54000 Nancy, France, and [c]Synchrotron SOLEIL-CNRS, L'Orme des Merisiers, Saint-Aubin, BP48, 91192 Gif-sur-Yvette, France. *Correspondence e-mail: emilie.gaudry@univ-lorraine.fr

Received 7 September 2018
Accepted 4 January 2019

Edited by P. A. Thiel, Iowa State University, USA

Keywords: complex intermetallic compounds; surfaces; bonding; density functional theory.

Clusters, *i.e.* polyhedral geometric entities, are widely used to describe the structure of complex intermetallic compounds. However, little is generally known about their physical significance. The atomic and electronic structures of the $Al_{13}TM_4$ complex intermetallic compounds (TM = Fe, Co, Ru, Rh) have been investigated using a wide range of *ab initio* tools in order to examine the influence of the chemical composition on the pertinence of the bulk structure description based on 3D clusters. In addition, since surface studies were found to be a relevant approach to address the question of cluster stability in complex phases, the interplay of the cluster substructure with the 2D surface is addressed in the case of the $Al_{13}Co_4(100)$ and $Al_{13}Fe_4(010)$ surfaces.

1. Introduction

A large variety of intermetallic crystal structures are based on polyhedral entities, often called 'clusters', as first introduced by F. A. Cotton in the early 1960s to describe compounds containing metal–metal bonds (Cotton & Walton, 1982). This approach is very useful to represent the structures of complex intermetallic phases, like intermetallic clathrates, but also quasicrystals, their crystalline approximants and related phases (Steinhardt & Jeong, 1996; Suck *et al.*, 2002; Abe *et al.*, 2004). Typical clusters found in quasicrystals include the Mackay (Sugiyama *et al.*, 1998), Bergman (Bergman *et al.*, 1957) and Tsai clusters (Takakura *et al.*, 2001), and numerous polyhedral shapes are used to describe complex intermetallics.

There is not usually a unique description of crystal structures in terms of structural building blocks. For example, a packing of pentagonal bipyramids was initially used by Henley to describe the $Al_{13}TM_4$ structure types (TM = Fe, Co, Ru, Rh, Fig. 1). Later, based on quantum chemistry calculations (Armbrüster *et al.*, 2011), these compounds were represented as columns of elongated clusters containing strong TM–Al–TM molecular groups, resembling the 3D 'cage-compound' structure of the intermetallic clathrates. Dong's cluster+glue model, describing the structure by the $[\text{icosahedron}](\text{glue})_{0,1}$ formula containing all the key information on alloy chemistry (Dong *et al.*, 2007), uses two types of icosahedral clusters for $Al_{13}Fe_4$: Al_9Fe_4 and Fe_2Al_{11} (Chen *et al.*, 2014). Finally, the $18 - n$ bonding scheme applied to $Al_{13}Os_4$ describes the structure by a stacking of Al_5 square pyramids and fluorite-type columns (Miyazaki *et al.*, 2017).

The question of cluster stability in complex intermetallic compounds was reviewed a few years ago in the case of quasicrystals (Steurer, 2006). Several studies mention the

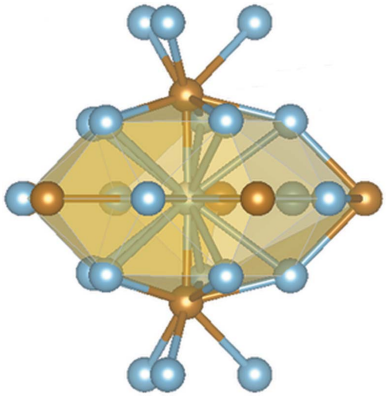

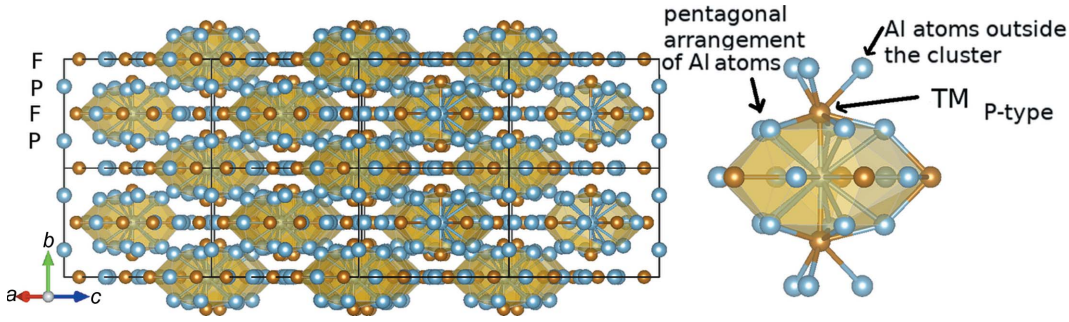

Figure 1
Left: $Al_{13}Fe_4$ bulk structure, highlighting (i) the description based on the stacking of atomic planes perpendicular to the [010] direction (F- and P-type planes) and (ii) the description based on the Henley-type clusters. Right: Henley-type cluster.

influence of the intrinsic cluster structure on the bulk physical properties, such as their mechanical properties (Feuerbacher *et al.*, 2001; Messerschmidt *et al.*, 1999) or their electronic conductivity (Janot & de Boissieu, 1994; Janot, 1996; Trambly de Laissardière *et al.*, 1997, 2006; Fujiwara, 1989; Fujiwara *et al.*, 1993; Zijlstra & Bose, 2003; Trambly de Laissardière & Fujiwara, 1994; Trambly de Laissardière & Mayou, 1997; Dolinšek *et al.*, 2000; Stadnik *et al.*, 2001; Widmer *et al.*, 2006; Zijlstra & Janssen, 2000; Trambly de Laissardière, 2003, 2009). Molecular dynamics based modelling of crack and dislocation propagation in simple quasiperiodic model structures (Mikulla *et al.*, 1998; Rösch *et al.*, 2004, 2005; Rudhart *et al.*, 2004) also questioned the role of clusters. Surface studies were found to be a pertinent approach to gain some insight into the question of cluster stability in quasicrystals (Dubois & Belin-Ferré, 2011; McGrath *et al.*, 2010, and references therein). When prepared by sputtering and annealing cycles, quasicrystalline surfaces usually produce large, atomically flat terraces. The patterns observed by scanning tunnelling microscopy (STM) are attributed to signatures of the dissected clusters at the surface (Krajčí & Hafner, 2005). This then suggests that the clusters in icosahedral quasicrystals are not stable sub-units that maintain their shapes at the surface. Do these conclusions present a general character among complex phases? Recently, several surfaces of a cage compound – namely the type-I clathrate BaAuGe – were investigated by a combination of experimental and theoretical techniques. It was found that these surfaces preserve the cluster substructure, which is stabilized by a charge transfer mechanism (Anand *et al.*, 2018*a*,*b*).

It follows that different surface behaviours occur among complex phases. In the following, we focus on the $Al_{13}TM_4$ complex intermetallics (TM = Fe, Co, Ru, Rh), usually considered as four-layer decagonal quasicrystalline approximants, because they present a layered structure and pentagonal atomic arrangements (Goldman & Kelton, 1993). Experimentally, using single-crystal surfaces prepared by cycles of sputtering and annealing, significant differences were found among the considered pseudo-tenfold $Al_{13}TM_4$ (TM = Fe, Co, Ru) surface structures (Fournée *et al.*, 2012; Ledieu *et al.*, 2013, 2017; Shin *et al.*, 2011), although common features were also observed. For all considered systems, the surface composition measured from XPS (X-ray photoelectron spectroscopy) as a function of surface sensitivity indicated no sign of chemical segregation. A surface plane selection is observed for all $Al_{13}TM_4$ pseudo-tenfold surfaces, highlighted by STM measurements which identified consecutive terraces separated by a unique step height equal to half the lattice parameter. However, the absence of surface reconstruction is not observed systematically: the LEED (low-energy electron diffraction) patterns of the $Al_{13}Co_4(100)$ and $Al_{13}Fe_4(010)$ surfaces show rectangular and oblique surface unit cells, respectively, with dimensions consistent with the bulk values, while the surface of $Al_{13}Ru_4(010)$ exhibits an atypical surface reconstruction, attributed to the occurrence of stripes running about 10° off the [001] direction. High-resolution STM images also identified different motifs at the surface for the different compounds (Fig. 2). Bipentagonal features are resolved at the $Al_{13}Co_4(100)$ surface while pairs of bright features are observed at the $Al_{13}Fe_4(010)$ surface, and fivefold motifs combined with pentagonal vacancies are visible at the $Al_{13}Ru_4(010)$ surface (Ledieu *et al.*, 2017).

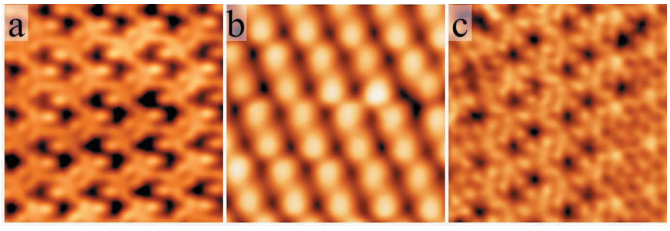

Figure 2
High-resolution STM images (6 × 6 nm). (*a*) o-$Al_{13}Co_4$ (V_b = −0.5 V), (*b*) $Al_{13}Fe_4$ (V_b = +1 V), (*c*) $Al_{13}Ru_4$ (V_b = −1.05 V).

For $Al_{13}Fe_4(010)$, the combination of theoretical calculations and experimental observations led to a model preserving the Henley-type clusters at the surface. The corresponding simulated STM images were in good agreement with the experimental images (Ledieu *et al.*, 2013). Further investigations based on dynamic LEED confirmed this result (Matilainen *et al.*, 2015). Several complementary techniques have been employed to reach a reliable model of the $Al_{13}Co_4(100)$ surface. The combination of STM, calculations based on density functional theory (DFT) and LEED converged towards a surface terminating at puckered layers (hereafter P-layers, Fig. 1) where on average all Al atoms are present and protruding Co atoms are missing (Shin *et al.*, 2011;

Fournée *et al.*, 2012). The surface structure showed heterogeneities, identified by STM, related to the partial occupancy of a few surface sites (Al 'glue' atoms, located in between Al bipentagonal motifs). The combination of surface X-ray diffraction and DFT pointed towards the same surface model, with partial occupancies for surface Co sites slightly buried in the P-type plane (Gaudry *et al.*, 2016).

Whether or not clusters are preserved at the surface must be linked to the strength of their intrinsic bonds and, as such, is expected to strongly depend on the atomic and electronic structures of the considered compounds. While the dimensionality of the chemical bonding network in o-$Al_{13}Co_4$ and $Al_{13}Fe_4$ has been investigated on the basis of electrical transport measurements (Dolinšek & Smontara, 2011), no theoretical extensive and systematic comparison of the compounds in the $Al_{13}TM_4$ (TM = Co, Fe, Ru, Rh) series has been carried out so far. Our work is based on a wide range of *ab initio* tools, based on DFT, in order to investigate the influence of the chemical composition on the pertinence of a bulk structure description based on clusters. Electronic structure calculations, including band structure calculations, projected density of states and projected crystal orbital Hamilton populations, highlight the different bonding characters of Al–Al, Al–TM and TM–TM pairs and how they contribute to the bulk cohesion. Methods based on infinitesimal displacements and harmonic approximations emphasize the impact of the chemical composition on phonon properties. Anisotropic thermal displacements are analysed and the singular behaviour induced by the cage structure is shown. Altogether, our results are used to discuss the relevance of the cage- versus layer-based descriptions. Finally, the interplay between the 3D bulk atomic arrangements and the 2D surface is discussed, based on surface energy calculations, before we present the conclusion.

2. Computational details and methods

2.1. Bulk calculations

The ground-state properties of the $Al_{13}TM_4$ structures, with TM = Fe, Co, Ru or Rh, are deduced from calculations based on DFT, using the plane-wave *Vienna ab initio simulation package* (*VASP*) (Kresse & Hafner, 1993, 1994, 1996*a*,*b*). The interaction between the valence electrons and the ionic core is described using the projector-augmented wave (PAW) method (Blöchl, 1994; Kresse & Joubert, 1999) within the generalized gradient approximation (GGA-PBE) (Perdew *et al.*, 1996, 1997), considering the valences for the atoms to be $3s^23p^1$ (Al), $4s^13d^7$ (Fe), $4s^13d^8$ (Co), $4p^65s^14d^7$ (Ru) and $4p^65s^14d^8$ (Rh). Spin polarization is not taken into account, as it was shown to be unnecessary for such Al-rich complex intermetallic compounds (Mihalkovič & Widom, 2007; Shin *et al.*, 2011). Total energies are minimized until the energy differences become less than 10^{-5} eV (respectively, 10^{-8} eV) between two electronic cycles during the structural optimizations (respectively, phonon calculations). Atomic structures are relaxed until the Hellmann–Feynman forces are as low as 0.02 eV $Å^{-1}$. They are plotted using the *VESTA* software (Momma & Izumi, 2011).

Total energy calculations were performed using a cut-off energy (E_{cut}) and a number of *k*-points within the Brillouin zone so as to achieve an energy accuracy better than 0.1 meV per atom (E_{cut} = 450 eV, Monkhorst–Pack *k*-points grid = 9 × 7 × 5 or equivalent). The reciprocal-space sampling was increased for electronic structure calculations (17 × 13 × 9 Monkhorst–Pack *k*-points grid) and the tetrahedron method with Blöchl corrections was used for Brillouin zone integrations. For the phonon calculations with supercells (2 × 1 × 1 or equivalent), we used a smaller *k*-point grid (2 × 2 × 2), in agreement with the setup of Mihalkovič & Widom (2007).

The phonon frequencies and the thermal displacements are determined using force constants derived from the calculation of the dynamic matrix based on the finite displacement method implemented in the *Phonopy* software (Togo & Tanaka, 2015). We used small atomic displacements (±0.01 Å). No imaginary mode was detected. The ellipsoid software was used to convert the thermal displacement parameters from the Cartesian to the crystal coordinate system (Deringer *et al.*, 2014; George *et al.*, 2015).

We used the projected crystal orbital Hamilton population (pCOHP) approach, implemented in the *LOBSTER* code (Dronskowski & Bloechl, 1993; Deringer *et al.*, 2011; Maintz *et al.*, 2013, 2016) to analyse the chemical bonding. This method re-extracts Hamilton-weighted populations from plane-wave electronic structure calculations to develop a tool analogous to the crystal orbital Hamilton population (COHP) method (Deringer *et al.*, 2011). The electron wavefunctions are projected onto the atomic local basis used for the DFT calculations: 3*s*3*p* for Al, 4*s*3*d* for Co and Fe, 4*p*5*s*4*d* for Ru and Rh. The charge spilling, *i.e.* electrons which cannot be projected onto the local basis, is found to be between 1 and 3% (1.09% for $Al_{13}Rh_4$ and 2.79% for $Al_{13}Fe_4$).

2.2. Surface energy calculations

The surfaces have been modelled with seven-layer-thick symmetric slabs, separated by a void thickness (≃12 Å). Surface energies (γ_{clean}) were computed as a function of the Al chemical potential:

$$\gamma_{clean} = \frac{1}{2A}(E^{slab} - N_{Al}\mu_{Al} - N_{TM}\mu_{TM})$$

where E_{slab} is the total energy of the slab, μ_i and N_i the chemical potential and number of *i* species in the slab. The surface is considered to be in equilibrium with the underlying bulk, which constrains the chemical potentials in a range, *i.e.* $(17/13)\Delta H_f \leq \mu_{Al} - \mu_{Al}^{bulk} \leq 0$ for Al, where ΔH_f is the formation energy of the complex phase.

Our values of the chemical potentials for the elemental Al, Fe, Co, Ru and Rh bulk crystals are in good agreement with experimental data: −3.52 eV for face-centred cubic Al (experimental: −3.39 eV), −4.86 eV for centred cubic Fe (experimental: −4.28 eV), −5.17 and −6.76 eV for hexagonal compact Co and Ru, respectively (experimental: −4.39 and −6.74 eV, respectively) (Kittel, 1996). The resulting formation

energies for $Al_{13}TM_4$ compounds (TM = Fe, Co, Ru) are −0.329, −0.384, −0.522 eV per atom, respectively, in agreement with the values calculated by Mihalkovič & Widom (2004) (−0.349, −0.410, −0.548 eV per atom, respectively).

The $Al_{13}TM_4$ compounds have been identified as promising catalysts towards hydrogenation reactions (Armbrüster *et al.*, 2009, 2012; Piccolo, 2013; Piccolo & Kibis, 2015). Therefore, to investigate a possible modification of the surface structure during operating conditions (H_2 atmosphere), the surface energies of the hydrogenated surfaces (γ_{cover}) were evaluated by the sum of the clean surface energies (γ_{clean}) and those with adsorbed species (γ_{ads}) (Reuter *et al.*, 2002; Reuter & Scheffler, 2003; Posada-Pérez *et al.*, 2017): $\gamma_{cover} = \gamma_{clean} + \gamma_{ads}(P, T, N_{H_2})$ where P, T and $2 \times N_{H_2}$ are the pressure, temperature and number of hydrogen atoms adsorbed on the surface. A simple thermodynamic model was used to compute γ_{ads}:

$$\gamma_{ads} = \frac{1}{A}\{E^{slab\text{-}cover} - E^{slab} - N_{H_2}[E_{H_2} + \Delta\mu^0_{H_2}(T, P^0) + k_B T \ln(P/P^0)]\}$$

	o-$Al_{13}Co_4$				$Al_{13}TM_4$		
	x	y	z		x	y	z
Γ	0	0	0	Γ	0	0	0
R	1/2	1/2	1/2	C	x_C	x_C	0
S	1/2	1/2	0	$C2$	$-x_C$	$1-x_C$	0
T	0	1/2	1/2	$Y2$	−1/2	1/2	0
U	1/2	0	1/2	$M2$	−1/2	1/2	1/2
X	1/2	0	0	D	$-x_D$	$1-x_D$	1/2
Y	0	1/2	0	$D2$	x_D	x_D	1/2
Z	0	0	1/2	A	0	0	1/2
				$L2$	0	1/2	1/2
				$V2$	0	1/2	0

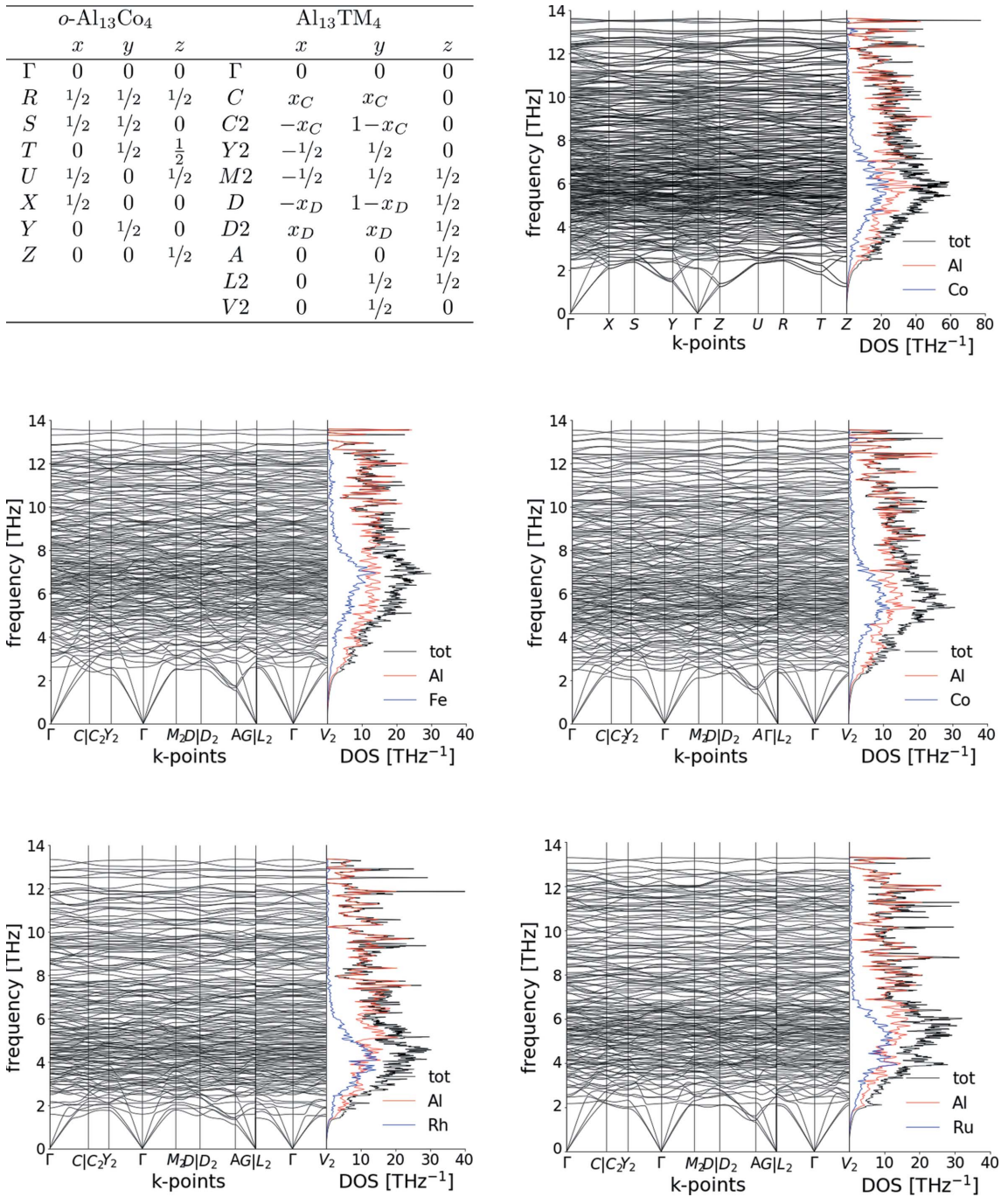

Figure 3
Phonon band structures and densities for o-$Al_{13}Co_4$ and monoclinic $Al_{13}TM_4$ compounds (TM = Co, Fe, Ru, Rh).

where E_{H_2} is the energy of H_2 in vacuum, and $\Delta\mu_{H_2}$ is the chemical potential of H_2 calculated as $\Delta\mu_{H_2} = -k_B T \ln Z$ where Z is the partition function of the gas-phase H_2 molecule and k_B is the Boltzmann constant. In the latter partition function, we only consider the translational and rotational contributions.

3. Bulk structures

3.1. Atomic structures

The $Al_{13}TM_4$ structures belong to the $C2/m$ space group (102 and 51 atoms per cell for the conventional and unit cells, respectively). We also considered the $Al_{13}Co_4$ orthorhombic phase (o-$Al_{13}Co_4$), which crystallizes in the $Pmn2_1$ space group, with 102 atoms per cell. These two structures share similarities. They are described as a stacking of flat (F) and puckered (P) layers along the pseudo-tenfold axis ([010] for monoclinic crystals, [100] for the orthorhombic one). As mentioned in Section 1, these structures are also described by a stacking of clusters. In the following, the term 'cluster' refers to the Henley-type cluster (Fig. 1), *i.e.* the pentagonal bipyramid.

The cell parameters deduced from the structural optimizations are gathered in Table 1. They are in good agreement with the experimental data. Here, full occupancies were considered in the theoretical approach, while partial occupancies are experimentally observed (Grin *et al.*, 1994*a*,*b*) and contribute to the stability of the compounds (Mihalkovič & Widom, 2007).

The relative differences $\Delta x = (|x_{calc} - x_{exp}|)/x_{exp}$ are smaller than 1% (respectively, 0.2%) for cell lengths (respectively, β angle). One exception is found for the $Al_{13}Rh_4$ compound (Δa and Δb are between 4 and 5%) (Chaudhury & Suryanarayana, 1983).

3.2. Phonon band structures

To evaluate the anisotropic displacement parameters, phonon calculations have been carried out. The resulting phonon band spectra are presented in Fig. 3 for o-$Al_{13}Co_4$ and monoclinic $Al_{13}TM_4$ (TM = Co, Fe, Ru, Rh). There are 153 and 306 branches in the phonon band structure, corresponding to the $3 \times N$ degrees of freedom in the primitive unit cell for the monoclinic and orthorhombic structures, respectively. No band gap is observed, the optic modes arising from around 1.1–1.5 THz, in the A-point (respectively, Z-point) of the Brillouin zone for monoclinic (respectively, orthorhombic) structures. No clear difference between the averaged group velocities calculated perpendicularly or within the pseudo-tenfold axis is observed.

The phonon densities of states show a Debye behaviour at low energies and a maximum located around 4–6 THz. The position of the maximum is shifted to lower energies when moving from $Al_{13}Co_4$ and $Al_{13}Fe_4$ to $Al_{13}Ru_4$ and $Al_{13}Rh_4$, because 4*d* metals are heavier. For $Al_{13}Co_4$, our results for the vibrational density of states are in agreement with the experimentally measured ones (Mihalkovič *et al.*, 2000), and compare quite well with those reported by Mihalkovič & Widom (2007). However, in the latter case, the consideration of a single Al vacancy leads to a slight excess in the density of states at low frequency, which is not observed here because full occupancies were considered.

Table 1
Cell parameters resulting from structural optimization, for $Al_{13}TM_4$ monoclinic structures ($C2/m$ space group) with TM = Fe, Co, Ru, Rh.

The case of the orthorhombic structure for $Al_{13}Co_4$ ($Pmn2_1$ space group) is considered as well.

		a (Å)	*b* (Å)	*c* (Å)	β (°)
$Al_{13}Fe_4$	Calculated	15.43	8.03	12.43	107.70
	Experimental (Grin *et al.*, 1994*b*)	15.492	8.078	12.471	107.69
	Experimental (Kazumasa *et al.*, 2012)	15.495	8.089	12.485	107.70
$Al_{13}Co_4$	Calculated	15.14	8.19	12.40	107.73
	Experimental (Hudd & Taylor, 1962)	15.183	8.122	12.340	107.81
o-$Al_{13}Co_4$	Calculated	8.195	12.40	14.43	90
	Experimental (Grin *et al.*, 1994*a*)	8.158	12.342	14.452	90
$Al_{13}Ru_4$	Calculated	15.94	8.30	12.82	107.76
	Experimental (Edshammar, 1965)	15.862	8.188	12.736	107.77
	Experimental (Murao *et al.*, 2011)	15.860	8.192	12.742	107.77
$Al_{13}Rh_4$	Calculated	15.64	8.45	12.79	107.92
	Experimental (Chaudhury & Suryanarayana, 1983)	16.36	8.05	12.79	107.77

The previous phonon calculations were used to calculate the U_{ij} anisotropic thermal displacements. Larger anisotropic displacements are found for several Al atoms in the flat plane, the largest one being observed for the Al atom of the TM–Al–TM molecular group, with values for $U_{pseudo\text{-}tenfold}/(U_\perp^2 + U_{\perp'}^2)^{1/2}$ between 0.1 and 0.3 (Fig. 4). This is in agreement with the bonding picture, the Al atom located in the cluster centre being involved in strong bonds within the neighbouring Al_5TM atomic arrangements located in the P-type plane above or below, while the covalent-like interactions with the surrounding atoms in the flat plane are found to be negligible (see Section 4).

3.3. Electronic band structures

At low energy, the electronic structures of the $Al_{13}TM_4$ compounds (Fig. 5) present a parabolic dispersion, due to the

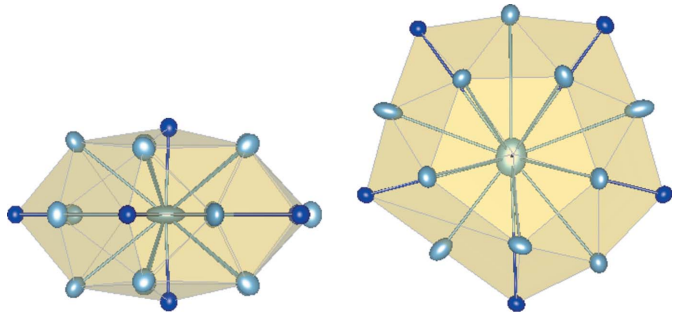

Figure 4
Top and side views of the anisotropic displacements for atoms located in the Henley-type cluster ($Al_{13}Co_4$ compound).

Table 2
Position of the *d*-band maximum and density of states at the Fermi energy for the considered compounds.

	$Al_{13}Fe_4$	o-$Al_{13}Co_4$	$Al_{13}Ru_4$	$Al_{13}Rh_4$
max(*d*-TM) (eV)	−1.29	−1.98	−2.50	−3.49
$n(E_F)$ (states per atom per eV)	0.286	0.316	0.179 0.219 (Manh *et al.*, 1995)	0.254

free electron behaviour of the *sp*-like states. The orange colour of the bands shows the predominance of Al-*sp* states over TM-*sp* states. At higher energy, a strong maximum appears in the density of states (DOS), caused by localized and weakly dispersive TM-*d* states. This is in agreement with previous calculations (Mihalkovič & Widom, 2007; Manh *et al.*, 1995). The uniform colour of bands suggests a strong hybridization between Al-*sp* states and TM-*sp* states as well as between Al-*sp* states and TM-*d* states. A minimum in the DOS close to the Fermi energy (a pseudo-gap) is visible for all compounds, contributing to their stabilization (Mizutani & Sato, 2017; Trambly de Laissardière *et al.*, 2005). For $Al_{13}Ru_4$ the DOS at the Fermi energy is reduced to 35% compared with the value for $Al_{13}Fe_4$, in agreement with specific heat measurements (Wencka *et al.*, 2017) (Table 2).

The electron per atom ratio (e/a) using the atomic values recently computed by Mizutani *et al.* (Mizutani & Sato, 2017; Mizutani *et al.*, 2013; Mizutani, 2010) (1.00 for Rh, 1.03 for Co, 1.04 for Ru, 1.05 for Fe and 3.01 for Al) is 2.5 for the $Al_{13}TM_4$ compounds, *i.e.* slightly larger than the values usually observed for Hume-Rothery phases (Ferro & Saccone, 2008), which classifies them as polar intermetallics. The presence of the pseudo-gap may then be due to a combination of the Hume-Rothery stabilization mechanism with hybridization effects, as already highlighted for Al_9Co_2 (Trambly de Laissardière *et al.*, 2005).

4. Network of chemical bonds

The bonding network in the $Al_{13}TM_4$ compounds is investigated in order to gain some insight into the various surface structures observed, the broken bond model being largely employed to account for surface energies (Ruvireta *et al.*, 2017).

4.1. Chemical bonding analysis

The chemical bond analysis based on the COHP curves and their integrated values (ICOHP, Table 3) revealed that the strongest bonds are homonuclear Al–Al bonds, located within the F-type atomic plane and ensuring the connection between clusters (Fig. 6). The strength of these bonds is rather high (larger than 2 eV per bond), despite quite large Al–Al distances (larger than 2.5 Å). This is consistent with the idea that the metallic bond is very closely related to the covalent

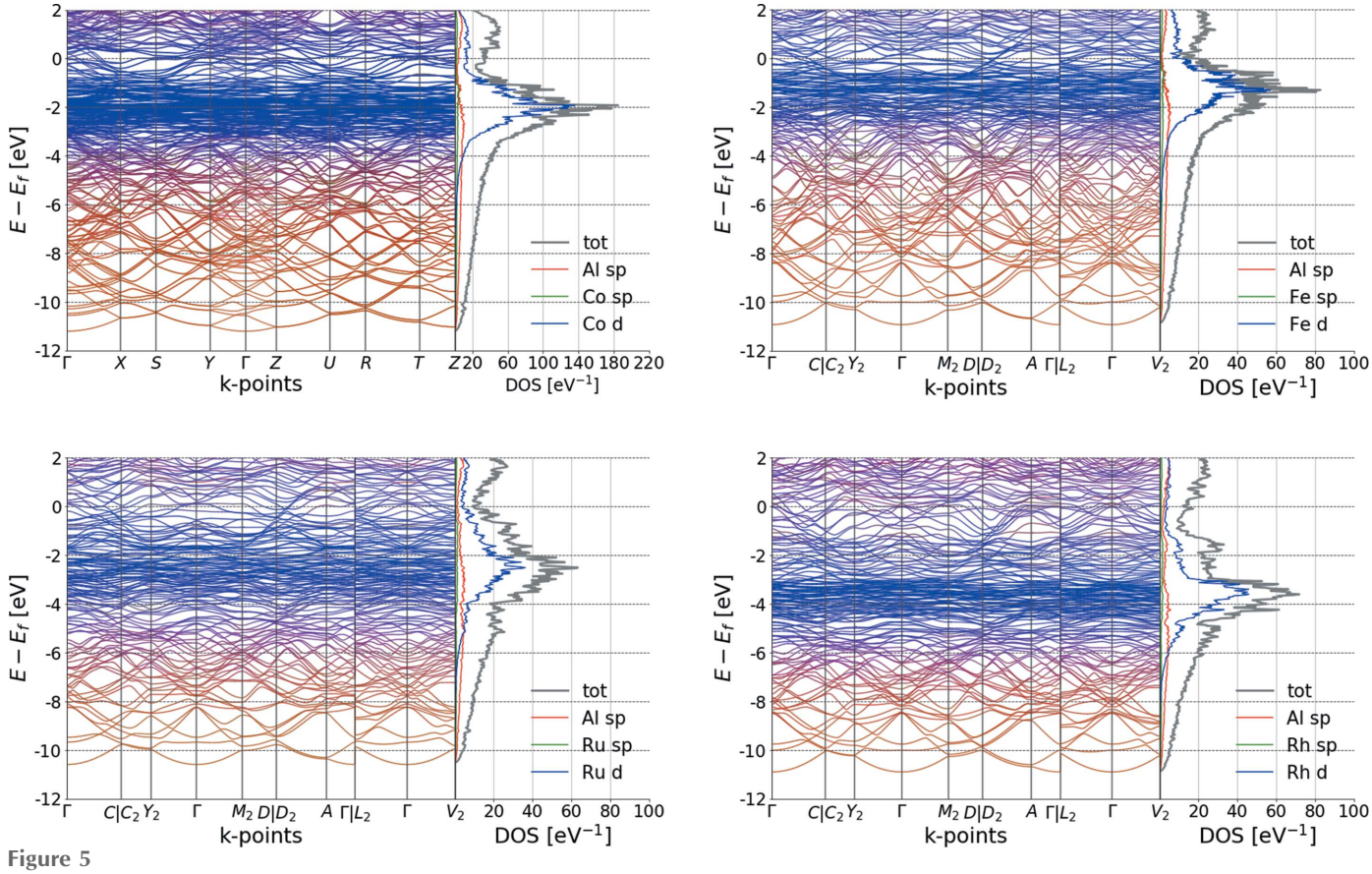

Figure 5
Band structures of the o-$Al_{13}Co_4$ and monoclinic $Al_{13}TM_4$ compounds (TM = Fe, Ru, Rh).

Table 3
Average ICOHP/bond values (eV per bond), along with the corresponding average distance (in parentheses, in Å), for the strongest Al–Al, TM–TM and Al–TM bonds in $Al_{13}TM_4$ compounds.

	Al–Al	Al–TM	TM–TM
$Al_{13}Fe_4$	2.60 (2.54 Å)	1.83 (2.35 Å)	0.23 (2.91 Å)
o-$Al_{13}Co_4$	2.46 (2.61 Å)	1.62 (2.27 Å)	0.18 (2.89 Å)
$Al_{13}Ru_4$	2.71 (2.57 Å)	2.29 (2.44 Å)	0.40 (3.04 Å)
$Al_{13}Rh_4$	2.40 (2.57 Å)	2.01 (2.38 Å)	0.18 (3.02 Å)

(shared-electron-pair) bond, and that each atom in a metal may be considered as forming covalent bonds with neighbouring atoms, the covalent bonds resonating among the available interatomic positions (Pauling, 1947). The shortest Al–TM distances also lead to strong bonds. They are identified as those of the TM–Al–TM molecular group located inside the cluster, oriented parallel to the pseudo-tenfold axis, connecting the F- and P-type atomic planes, in agreement with the previous analysis by Grin *et al.* (Armbrüster *et al.*, 2011), and consistent with the NMR study by Jeglič *et al.* (2009, 2010). Very weak TM–TM bonds are found (≃0.2 eV per bond), with bonding distances close to 3 Å.

4.2. Cage- versus layer-based description

To probe the stacked-layer structure of the $Al_{13}TM_4$ periodic decagonal approximants, we evaluate the P-type in-plane ($S_{in}^{P\text{-type}}$) and inter-plane (S_{out}) bonding capacities by

$$S_{in}^{P\text{-type}} = \frac{1}{2}\sum_{i\in P\text{-type}}\sum_{j\in P\text{-type}}(-\text{ICOHP})_{ij} \quad (1)$$

$$S_{out} = \sum_{i\in P\text{-type}}\sum_{j\in F\text{-type}}(-\text{ICOHP})_{ij}. \quad (2)$$

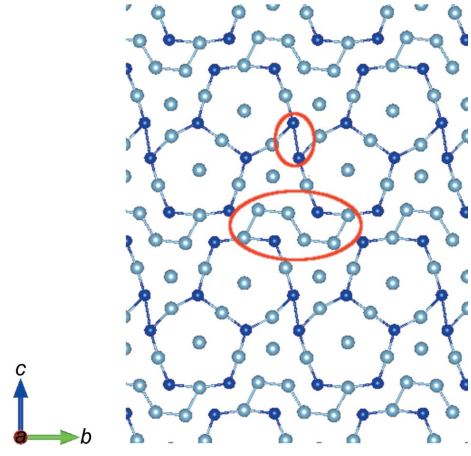

Figure 6
Structure of the o-$Al_{13}Co_4$ F-type plane highlighting the strongest Al–Al and Co–Co bonds (red circles), which are inter-cluster bonds, linking together bipentagonal atomic arrangements. Light blue = Al; dark blue = Co.

Table 4
Average ICOHP/bond values (eV per bond) and percentage contributions (the contributions of the bonding relative to a given atom are evaluated by the sum of the ICOHP/bond values of the nearest neighbouring interactions weighted by the respective bond frequencies) of the respective interactions to the net bonding capabilities around the TM atoms located in the P-type atomic plane.

Three types of Al neighbours are considered: the Al atoms within the TM–Al–TM molecular group, the surrounding Al atoms in the P-type plane (pentagonal arrangement), and those outside the cluster, in the F-type plane (Fig. 1).

	TM–Al (TM–Al–TM)		$TM–Al_{F\text{-type}}$		$TM–Al_{P\text{-type}}$	
	eV per bond	%	eV per bond	%	eV per bond	%
$Al_{13}Fe_4$	1.83	16.8	1.14	31.3	1.13	51.9
o-$Al_{13}Co_4$	1.62	16.0	1.03	30.6	1.08	53.3
$Al_{13}Ru_4$	2.30	16.6	1.41	30.5	1.47	52.3
$Al_{13}Rh_4$	2.01	16.1	1.27	30.4	1.34	53.6

The ratio $S_{in}/(S_{in}+S_{out})$ is calculated to be 24.5%, 26.8%, 24.4% and 28.4% for TM = Fe, Co, Ru, Rh, respectively. These results are consistent with the conclusions of Dolinšek & Smontara (2011), based on anisotropic resistivity measurements, stating that the stacked-layer description in terms of 2D atomic planes should only be regarded as a convenient geometrical approach to describe structures of the $Al_{13}TM_4$ quasicrystalline approximants, whereas their physical properties are those of true 3D solids.

Cluster stability is evaluated through the bonding capacity of TM atoms located in the P-type planes ($TM_{P\text{-type}}$). Such atoms are bounded to three different types of Al neighbours: the Al atom within the TM–Al–TM molecular group, the surrounding Al atoms, located in the P-type plane (pentagonal arrangement), and the ones outside the cluster, within the flat plane (Fig. 1). Our results are presented in Table 4. For all compounds, the contributions to the bonding capabilities of the TM–Al–TM molecular group are around 16–17%. It is the largest for $Al_{13}TM_4$ with TM = Fe, Ru, because the corresponding states show almost no anti-bonding for TM = Fe, Ru (Fig. 7), while they are slightly anti-bonding for TM = Co, Rh. For all compounds, the intra-cluster Al–$TM_{P\text{-type}}$ interactions

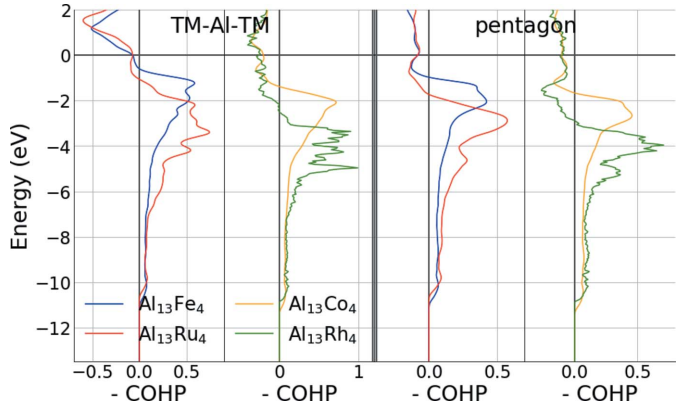

Figure 7
COHP curves for the TM–Al bonds of the TM–Al–TM molecular group, along with those showing the interactions of $TM_{P\text{-type}}$ atoms with the surrounding Al atoms in the P-type plane (Al pentagonal arrangements).

contribute 69–70% to the bonding capabilities. More than 50% of these interactions are attributed to the closest Al pentagonal arrangement, even if slight anti-bonding TM–$Al_{P\text{-type}}$ interactions at the Fermi level are revealed by the COHP curves. Intra-cluster contributions to the bonding capabilities of $TM_{P\text{-type}}$ atoms are the strongest for $Al_{13}Fe_4$, and the lowest for o-$Al_{13}Co_4$ and $Al_{13}Rh_4$. An intermediate case is that of $Al_{13}Ru_4$, with Al–$TM_{P\text{-type}}$ bonds within the $TM_{P\text{-type}}$–Al–$TM_{P\text{-type}}$ group as strong as those in $Al_{13}Fe_4$, while the strengths of TM–$Al_{F\text{-type}}$ bonds are similar in $Al_{13}Ru_4$, o-$Al_{13}Co_4$ and $Al_{13}Rh_4$.

4.3. Bonding strengths and bonding distances

Finally, when looking at the variation of bonding strength as a function of bonding distance (Fig. 8), an exponential behaviour is observed, in agreement with the exponential decrease in the bond number n with bonding distance D_n (in Å) initially proposed by Pauling (1947, 1960): $D_n = D_1 - A \times \log_{10} n$ [equation (29) in Herman (1999)].

5. Bonding network and pseudo-tenfold surfaces

From the bonding analysis, the P-type in-plane bonding capacities are evaluated to be in the range 20–30%. The clusters are found to be rather stable entities, the intra-cluster Al–$TM_{P\text{-type}}$ interactions contributing 69–70% to the $TM_{P\text{-type}}$ bonding capabilities. In the following, we discuss the consistency of these results with the pseudo-tenfold surface structures identified so far.

5.1. Clean surfaces

Two surface models are considered in the following. The A-type model preserves the Henley-type clusters at the surface, while the B-type surface model terminates at P-layers where on average all Al atoms are present and protruding Co atoms are missing. The surface energies of these two models are plotted in Fig. 9. The A-type model, preserving the cluster structure at the surface, is found to be the most stable within a large domain of chemical potentials, for both $Al_{13}Co_4$(100) and $Al_{13}Fe_4$(010), in agreement with the bonding situation of the compounds. However, the surface structure observed for $Al_{13}Co_4$(100) is the B-type one, corresponding to the narrow range in the Al-rich region.

The surface structures of the $Al_{13}TM_4$ compounds with TM = Co and Fe reflect the duality between the description of the structure based (i) on a stacking of atomic planes (F- and P-type) perpendicular to the pseudo-tenfold direction, mirroring the periodic stacking of atomic planes with quasi-periodic in-plane atomic order found in decagonal quasicrystals, and (ii) on a stacking of Henley-type clusters. A dense Al-rich surface was identified for o-$Al_{13}Co_4$(100) and a highly corrugated surface, based on the preservation of the cluster structure at the surface, for m-$Al_{13}Fe_4$(010). They are consistent with the stronger character of intra-cluster bonds of m-$Al_{13}Fe_4$ compared with o-$Al_{13}Co_4$. They are also consistent with the slightly stronger in-plane bonding capacities of the $Al_{13}TM_4$ (TM = Fe, Co) P-type planes: 24.5% and 26.8% for m-$Al_{13}Fe_4$ and o-$Al_{13}Co_4$, respectively.

Compared with the related m-$Al_{13}Fe_4$(010) and o-$Al_{13}Co_4$(100) surfaces where superstructures are absent, the reconstruction observed for m-$Al_{13}Ru_4$(010) is thought to act as a strain relief mechanism. Here, the Ru atoms located in the P-type atomic plane are strongly bonded to the Al atom of the Ru–Al–Ru molecular group: 2.30 eV per bond, but a bonding capacity similar to that of m-$Al_{13}Fe_4$(010), *i.e.* 16.6%. However, the surface structures of m-$Al_{13}Fe_4$(010) and m-$Al_{13}Ru_4$(010) present quite large differences, since a reconstruction is observed in the case of m-$Al_{13}Ru_4$(010).

5.2. Surface under hydrogen atmosphere

Both $Al_{13}Co_4$ and $Al_{13}Fe_4$ compounds have been identified as promising catalysts for hydrogenation reactions (Armbrüster *et al.*, 2009, 2012; Piccolo, 2013; Piccolo & Kibis, 2015). The performances of the catalysts are attributed to the Al_5TM atomic arrangements at the surface, in agreement with the site isolation concept. While such atomic arrangements have been experimentally observed for m-$Al_{13}Fe_4$(010), the surface structure determined so far under ultra-high vacuum for

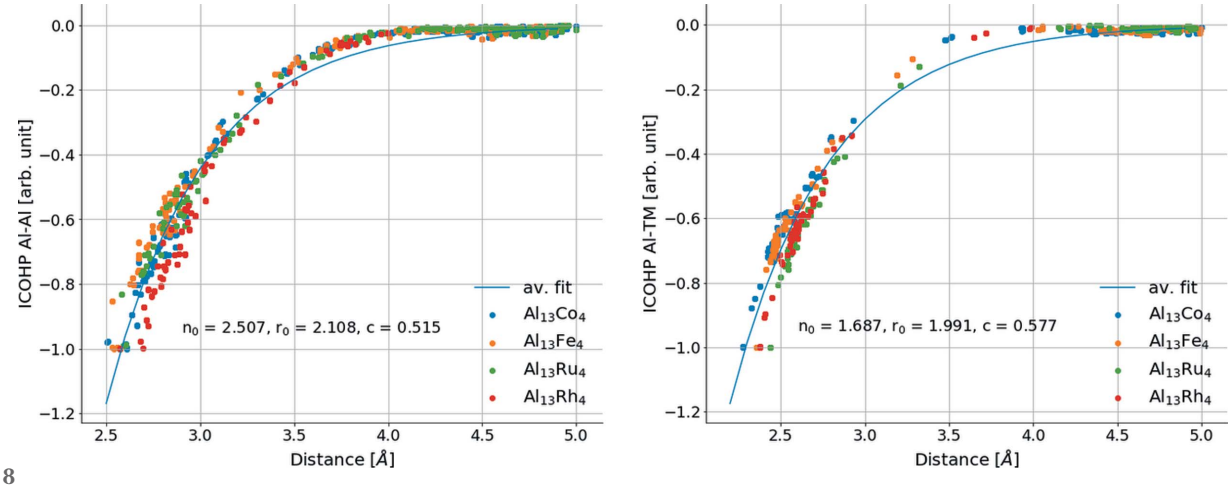

Figure 8
Bonding strength of Al–Al bonds in $Al_{13}TM_4$ compounds as a function of the distance. The fit uses the function $n_0 \exp[(r_0 - r)/c]$.

o-$Al_{13}Co_4$(100) consists of a dense Al-rich plane, leading to higher barriers for hydrogenation reactions (Krajčí & Hafner, 2011; Kandaskalov *et al.*, 2017).

Experimental conditions are known to have a strong effect on the surface structures. For example, slight deviations from an ordered alloy's ideal stoichiometry in the subsurface or bulk region can drastically affect the surface composition (Ruban, 2002; Blum *et al.*, 2002). Such effects have been observed on o-$Al_{13}Co_4$(100) using two single crystals grown by two different techniques, which may present slightly different bulk compositions (within the stability range of the o-$Al_{13}Co_4$ phase) (Fournée *et al.*, 2012). However, in both cases, the surface is Al rich and no Co atoms were found to protrude at the surface.

When used as catalysts, the surface structure may evolve under operating conditions. In particular, exothermic adsorption on solid surfaces is known to reduce their surface energy (Mathur *et al.*, 2005). In the following, we evaluate the modification of the surface energy due to the adsorption of atomic hydrogen. We focus on o-$Al_{13}Co_4$(100) using the two previous surface models (A- and B-type models). We consider two different coverages (4 and 8 atomic H per surface cell, Fig. 10). Atomic hydrogen is adsorbed on the most favourable adsorption sites (Krajčí & Hafner, 2011; Kandaskalov *et al.*, 2014). The adsorption leads to a decrease in the surface energy, for temperatures below 400 and 200 K for the A- and B-type models, respectively. The stabilization is higher for the A-type model, because atomic hydrogen is more strongly adsorbed on the A-type model. The relative stabilization of the A-type model compared with the B-type one is found to be 0.07 and 0.14 J m^{-2} for the two considered coverages, respectively.

The surface energy difference calculated between the A- and B-type models is 0.14 J m^{-2} for $\mu_{Al} = \mu_{Al}^{bulk}$, *i.e.* larger or equal to the relative stabilization of the A-type model compared with the B-type one, when $\mu_{Al} = \mu_{Al}^{bulk}$, and for the considered adsorption configurations and coverages. For small atomic hydrogen coverages (four atoms per surface cell), our calculations, realized with the PBE approach, suggest that the considered surface structures are rather stable. However, larger atomic hydrogen coverages are likely to modify the surface structure.

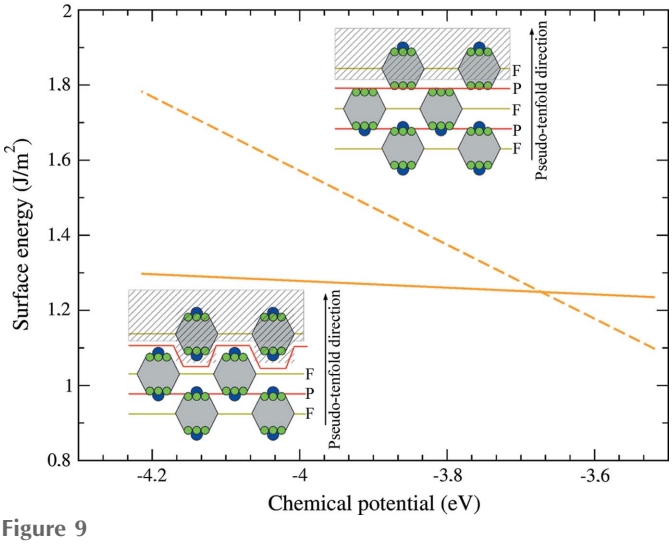

Figure 9
Surface energy of the A- (full line) and B-type (dashed line) models, calculated for o-$Al_{13}Co_4$(100).

6. Conclusion

We reported a systematic investigation of the electronic structure, phonon properties and chemical bonding network of bulk $Al_{13}TM_4$ compounds (TM = Co, Fe, Ru, Rh). Electronic structure calculations highlight rather strong hybridization. The strong TM–Al–TM bond within the Henley-type cluster leads to a strong anisotropy in the thermal displacement of the central Al atom. From the bonding analysis, the clusters are found to be rather stable entities, the intra-cluster $Al–TM_{P\text{-type}}$ interactions contributing 69–70% to the $TM_{P\text{-type}}$ bonding capabilities.

Structural differences between the o-$Al_{13}Co_4$(100) and m-$Al_{13}Fe_4$(010) surfaces have been observed for several different samples, different growth modes and for quite different annealing temperatures: bipentagonal motifs are systematically observed for o-$Al_{13}Co_4$(100), whereas they are never resolved in the case of m-$Al_{13}Fe_4$(010). The calculated

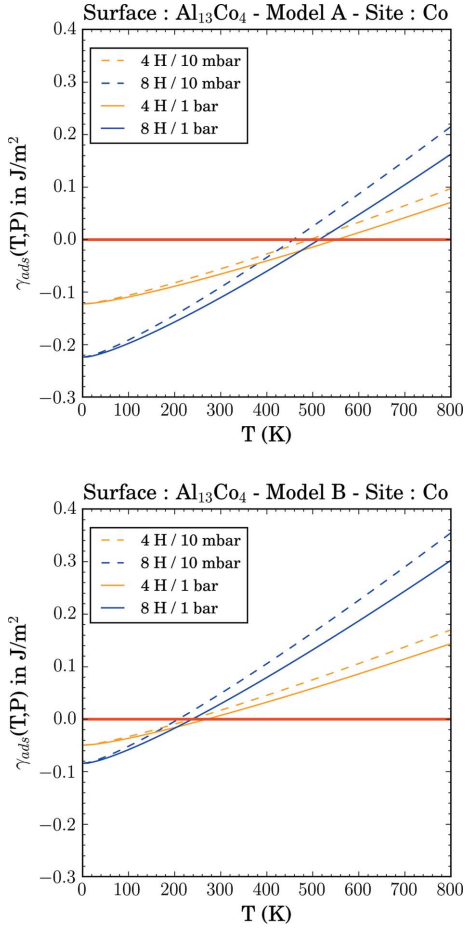

Figure 10
Modification of the o-$Al_{13}Co_4$(100) surface energy (γ_{ads}) with atomic hydrogen adsorbates, for two different coverages, as a function of temperature and pressure.

strengths of the Al–TM bonds within the TM–Al–TM molecular groups provide an understanding of the different surface structures observed. Since intra-cluster bonds are stronger for m-$Al_{13}Fe_4$ compared with o-$Al_{13}Co_4$, and in-plane bonding capacities of the P-type planes are stronger for o-$Al_{13}Co_4$ compared with m-$Al_{13}Fe_4$, Henley-type clusters are preserved at the m-$Al_{13}Fe_4$(010) surface while they are truncated at the o-$Al_{13}Co_4$(100) surface.

The possible interactions with adsorbates lead to a decrease in the calculated surface energies, at low temperatures ($T <$ 400–500 K and $T <$ 200–300 K for the A- and B-type models, respectively). The stabilization depends on the chemical potentials of the adsorbate, as well as on those of the Al and TM atoms. This highlights the importance of *operando* conditions when considering applications for these surfaces.

Nevertheless, the specific atomic arrangements at the surface induced by the intrinsic cluster substructure of complex intermetallic compounds affect the surface properties. Several adsorption studies highlight the role of specific sites resulting from the cut by the surface plane through the cluster units identified in the bulk solid (Unal *et al.*, 2009; Fournée *et al.*, 2014; Ledieu *et al.*, 2009; Krajčí & Hafner, 2008). On fivefold Al-based quasicrystalline surfaces, it leads to the two famous 'dark stars' and 'white flowers' sites (Unal *et al.*, 2009), which are identified as favourable atomic and molecular adsorption sites (Cai *et al.*, 2003; McGrath *et al.*, 2002). On approximant and related phases, signatures of the cluster substructure at the surface also lead to specific chemically active sites. For example, a possible reaction path for the semi-hydrogenation of acetylene on o-$Al_{13}Co_4$(100), identified as a performant catalyst for this reaction (Armbrüster *et al.*, 2009, 2012), is predicted to involve the protruding clusters ($CoAl_5$ ensemble) (Krajčí & Hafner, 2011). Given the structural variety of complex intermetallics, described by stackings of very diversified clusters naturally present in the bulk structure, we can hope to control the surface properties by the selection of clusters that emerge at the surface as active centres, giving rise to multiple applications at the nanoscale.

Funding information

This work was supported by the European Integrated Center for the Development of New Metallic Alloys and Compounds. High Performance Computing resources were partially provided by GENCI under the allocation 99642, as well as the EXPLOR centre hosted by the Université de Lorraine (allocation 2017M4XXX0108). This work was supported by the French PIA project *Lorraine Université d'Excellence*, reference ANR-15-IDEX-04-LUE.

References

Abe, E., Yan, Y. & Pennycook, S. J. (2004). *Nat. Mater.* **3**, 759–767.
Anand, K., Allio, C., Krellner, C., Nguyen, H. D., Baitinger, M., Grin, Y., Ledieu, J., Fournée, V. & Gaudry, E. (2018*a*). *J. Phys. Chem. C*, **122**, 2215–2220.
Anand, K., Allio, C., Krellner, C., Nguyen, H. D., Baitinger, M., Grin, Y., Ledieu, J., Fournée, V. & Gaudry, E. (2018*b*). *J. Phys. Chem. C*, **122**, 29298–29306.
Armbrüster, M., Kovnir, K., Friedrich, M., Teschner, D., Wowsnick, G., Hahne, M., Gille, P., Szentmiklósi, L., Feuerbacher, M., Heggen, M., Girgsdies, F., Rosenthal, D., Schlögl, R. & Grin, Y. (2012). *Nat. Mater.* **11**, 690–693.
Armbrüster, M., Kovnir, K., Grin, Y. & Schlögl, R. (2011). *Complex Metallic Alloys*, edited by J.-M. Dubois & E. Belin-Ferré. Weinheim: Wiley.
Armbrüster, M., Kovnir, K., Grin, Y., Schlögl, R., Gille, P., Heggen, M. & Feuerbacher, M. (2009). Ordered cobalt–aluminium and iron–aluminium intermetallic compounds as hydrogenation catalysts. Patent No. 09157875.7.
Bergman, G., Waugh, J. L. T. & Pauling, L. (1957). *Acta Cryst.* **10**, 254–259.
Blöchl, P. E. (1994). *Phys. Rev. B*, **50**, 17953–17979.
Blum, V., Hammer, L., Schmidt, C., Meier, W., Wieckhorst, O., Müller, S. & Heinz, K. (2002). *Phys. Rev. Lett.* **89**, 266102.
Cai, T., Ledieu, J., McGrath, R., Fournée, V., Lograsso, T., Ross, A. & Thiel, P. (2003). *Surf. Sci.* **526**, 115–120.
Chaudhury, Z. & Suryanarayana, C. (1983). *J. Less-Common Met.* **91**, 181–187.
Chen, H., Luo, L., Qiang, J., Wang, Y. & Dong, C. (2014). *Philos. Mag.* **94**, 1463–1477.
Cotton, F. & Walton, R. A. (1982). *Multiple Bonds Between Metal Atoms.* New York: John Wiley & Sons.
Deringer, V. L., Stoffel, R. P., Togo, A., Eck, B., Meven, M. & Dronskowski, R. (2014). *CrystEngComm*, **16**, 10907–10915.
Deringer, V. L., Tchougréeff, A. L. & Dronskowski, R. (2011). *J. Phys. Chem. A*, **115**, 5461–5466.
Dolinšek, J., Klanjšek, M., Apih, T., Smontara, A., Lasjaunias, J. C., Dubois, J. M. & Poon, S. J. (2000). *Phys. Rev. B*, **62**, 8862–8870.
Dolinšek, J. & Smontara, A. (2011). *Isr. J. Chem.* **51**, 1–11.
Dong, C., Wang, Q., Qiang, J. B., Wang, Y. M., Jiang, N., Han, G., Li, Y. H., Wu, J. & Xia, J. H. (2007). *J. Phys. D Appl. Phys.* **40**, R273–R291.
Dronskowski, R. & Bloechl, P. E. (1993). *J. Phys. Chem.* **97**, 8617–8624.
Dubois, J.-M. & Belin-Ferré, E. (2011). *Complex Metallic Alloys: Fundamentals and Applications.* Weinheim: Wiley-VCH.
Edshammar, L.-E. (1965). *Acta Chem. Scand.* **19**, 2124–2130.
Ferro, R. & Saccone, A. (2008). *Intermetallic Chemistry.* Oxford: Pergamon Elsevier.
Feuerbacher, M., Klein, H. & Urban, K. (2001). *Philos. Mag. Lett.* **81**, 639–647.
Fournée, V., Gaudry, E., de Weerd, M.-C., Diehl, R. D. & Ledieu, J. (2012). *MRS Proc.* **1517**, mrsf12-1517-kk02-07.
Fournée, V., Gaudry, E., Ledieu, J., de Weerd, M.-C., Wu, D. & Lograsso, T. (2014). *ACS Nano*, **8**, 3646–3653.
Fujiwara, T. (1989). *Phys. Rev. B*, **40**, 942–946.
Fujiwara, T., Yamamoto, S. & Trambly de Laissardière, G. (1993). *Phys. Rev. Lett.* **71**, 4166–4169.
Gaudry, E., Chatelier, C., McGuirk, G., Serkovic Loli, L. N., de Weerd, M., Ledieu, J., Fournée, V., Felici, R., Drnec, J., Beutier, G. & de Boissieu, M. (2016). *Phys. Rev. B*, **94**, 165406.
George, J., Wang, A., Deringer, V. L., Wang, R., Dronskowski, R. & Englert, U. (2015). *CrystEngComm*, **17**, 7414–7422.
Goldman, A. & Kelton, R. (1993). *Rev. Mod. Phys.* **65**, 213–230.
Grin, J., Burkhardt, U., Ellner, M. & Peters, K. (1994*a*). *J. Alloys Compd.* **206**, 243–247.
Grin, J., Burkhardt, U., Ellner, M. & Peters, K. (1994*b*). *Z. Kristallogr.* **209**, 479–487.
Herman, Z. S. (1999). *Theor. Comput. Chem.* **6**, 701–746.
Hudd, R. C. & Taylor, W. H. (1962). *Acta Cryst.* **15**, 441–442.
Janot, C. (1996). *Phys. Rev. B*, **53**, 181–191.
Janot, C. & de Boissieu, M. (1994). *Phys. Rev. Lett.* **72**, 1674–1677.

Jeglič, P., Heggen, M., Feuerbacher, M., Bauer, B., Gille, P. & Haarmann, F. (2009). *J. Alloys Compd.* **480**, 141–143.
Jeglič, P., Vrtnik, S., Bobnar, M., Klanjšek, M., Bauer, B., Gille, P., Grin, Y., Haarmann, F. & Dolinšek, J. (2010). *Phys. Rev. B*, **82**, 104201.
Kandaskalov, D., Fournée, V., Ledieu, J. & Gaudry, E. (2014). *J. Phys. Chem. C*, **118**, 23032–23041.
Kandaskalov, D., Fournée, V., Ledieu, J. & Gaudry, E. (2017). *J. Phys. Chem. C*, **121**, 18738–18745.
Kazumasa, S., Tatsuo, O. & Kenji, H. (2012). *Mater. Trans.* **53**, 1357–1362.
Kittel, C. (1996). *Introduction to Solid State Physics.*, 7th ed. New York: John Wiley & Sons.
Krajčí, M. & Hafner, J. (2005). *Phys. Rev. B*, **71**, 054202.
Krajčí, M. & Hafner, J. (2008). *Phys. Rev. B*, **77**, 134202.
Krajčí, M. & Hafner, J. (2011). *J. Catal.* **278**, 200–207.
Kresse, G. & Furthmüller, J. (1996*a*). *Comput. Mater. Sci.* **6**, 15–50.
Kresse, G. & Furthmüller, J. (1996*b*). *Phys. Rev. B*, **54**, 11169–11186.
Kresse, G. & Hafner, J. (1993). *Phys. Rev. B*, **47**, 558–561.
Kresse, G. & Hafner, J. (1994). *Phys. Rev. B*, **49**, 14251–14269.
Kresse, G. & Joubert, D. (1999). *Phys. Rev. B*, **59**, 1758–1775.
Ledieu, J., Gaudry, E., Fournée, V., Smerdon, J. & Diehl, R. (2017). *Z. Kristallogr. Cryst. Mater.* **232**, 629–645.
Ledieu, J., Gaudry, E., Loli, L. N. S., Villaseca, S. A., de Weerd, M.-C., Hahne, M., Gille, P., Grin, Y., Dubois, J.-M. & Fournée, V. (2013). *Phys. Rev. Lett.* **110**, 076102.
Ledieu, J., Krajčí, M., Hafner, J., Leung, L., Wearing, L., McGrath, R., Lograsso, T., Wu, D. & Fournée, V. (2009). *Phys. Rev. B*, **79**, 165430.
Maintz, S., Deringer, V. L., Tchougréeff, A. L. & Dronskowski, R. (2013). *J. Comput. Chem.* **34**, 2557–2567.
Maintz, S., Deringer, V. L., Tchougréeff, A. L. & Dronskowski, R. (2016). *J. Comput. Chem.* **37**, 1030–1035.
Manh, D. N., Paxton, A. T., Pettifor, D. G. & Pasturel, A. (1995). *Intermetallics*, **3**, 9–14.
Mathur, A., Sharma, P. & Cammarata, R. C. (2005). *Nat. Mater.* **4**, 186.
Matilainen, A., Pussi, K., Diehl, R. D., Hahne, M., Gille, P., Gaudry, É., Serkovic Loli, L. N., McGuirk, G. M., de Weerd, M., Fournée, V. & Ledieu, J. (2015). *Phys. Rev. B*, **92**, 014109.
McGrath, R., Ledieu, J., Cox, E., Haq, S., Diehl, R., Jenks, C., Fisher, I., Ross, A. & Lograsso, T. (2002). *J. Alloys Compd.* **342**, 432–436.
McGrath, R., Smerdon, J. A., Sharma, H. R., Theis, W. & Ledieu, J. (2010). *J. Phys. Condens. Matter*, **22**, 084022.
Messerschmidt, U., Bartsch, M., Feuerbacher, M., Geyer, B. & Urban, K. (1999). *Philos. Mag. A*, **79**, 2123–2135.
Mihalkovič, M., Elhor, H. & Suck, J.-B. (2000). *Mater. Sci. Eng. A*, **294–296**, 654–657.
Mihalkovič, M. & Widom, M. (2004). http://alloy.phys.cmu.edu/.
Mihalkovič, M. & Widom, M. (2007). *Phys. Rev. B*, **75**, 014207.
Mikulla, R., Gumbsch, P. & Trebin, H. (1998). *Philos. Mag. Lett.* **78**, 369–376.
Miyazaki, K., Yannello, V. & Fredrickson, D. (2017). *Z. Kristallogr. Cryst. Mater.* **232**, 487–496.
Mizutani, U. (2010). *Hume-Rothery Rules for Structurally Complex Alloy Phases.* Boca Raton: CRC Press.
Mizutani, U. & Sato, H. (2017). *Crystals*, **7**, 9.
Mizutani, U., Sato, H., Inukai, M. & Zijlstra, E. (2013). *Philos. Mag.* **93**, 3353–3390.
Momma, K. & Izumi, F. (2011). *J. Appl. Cryst.* **44**, 1272–1276.
Murao, R., Genba, M., Sugiyama, K. & Sun, W. (2011). *Mater. Trans.* **52**, 1344–1348.
Pauling, L. (1947). *J. Am. Chem. Soc.* **69**, 542–553.
Pauling, L. (1960). *The Nature of the Chemical Bond.* New York: Cornell University Press.
Perdew, J. P., Burke, K. & Ernzerhof, M. (1996). *Phys. Rev. Lett.* **77**, 3865–3868.
Perdew, J. P., Burke, K. & Ernzerhof, M. (1997). *Phys. Rev. Lett.* **78**, 1396.
Piccolo, L. (2013). *Chem. Commun.* **49**, 9149–9151.
Piccolo, L. & Kibis, L. (2015). *J. Catal.* **332**, 112–118.
Posada-Pérez, S., Viñes, F., Valero, R., Rodriguez, J. A. & Illas, F. (2017). *Surf. Sci.* **656**, 24–32.
Reuter, K. & Scheffler, M. (2003). *Phys. Rev. B*, **68**, 045407.
Reuter, K., Stampfl, C., Verónica Ganduglia-Pirovano, M. & Scheffler, M. (2002). *Chem. Phys. Lett.* **352**, 311–317.
Rösch, F., Rudhart, C., Gumbsch, P. & Trebin, H. (2003). *MRS Proc.* **805**, LL9.3.
Rösch, F., Rudhart, C., Roth, J., Trebin, H.-R. & Gumbsch, P. (2005). *Phys. Rev. B*, **72**, 014128.
Ruban, A. V. (2002). *Phys. Rev. B*, **65**, 174201.
Rudhart, C., Gumbsch, P. & Trebin, H. (2003). *MRS Proc.* **805**, LL9.2.
Ruvireta, J., Vega, L. & Viñes, F. (2017). *Surf. Sci.* **664**, 45–49.
Shin, H., Pussi, K., Gaudry, E., Ledieu, J., Fournée, V., Alarcón Villaseca, S., Dubois, J.-M., Grin, Y., Gille, P., Moritz, W. & Diehl, R. (2011). *Phys. Rev. B*, **84**, 085411.
Stadnik, Z. M., Purdie, D., Baer, Y. & Lograsso, T. A. (2001). *Phys. Rev. B*, **64**, 214202.
Steinhardt, P. J. & Jeong, H.-C. (1996). *Nature*, **382**, 431–433.
Steurer, W. (2006). *Philos. Mag.* **86**, 1105–1113.
Suck, J., Schreiber, M. & Haussler, P. (2002). *Quasicrystals: Introduction to Structure, Physical Properties, and Application*, edited by Ch. Janot & J.-M. Dubois, ch. 8, pp. 183–198. Berlin: Springer.
Sugiyama, K., Kaji, N. & Hiraga, K. (1998). *Acta Cryst.* C**54**, 445–447.
Takakura, H., Guo, J. & Tsai, A. (2001). *Philos. Mag. Lett.* **81**, 411–418.
Togo, A. & Tanaka, I. (2015). *Scr. Mater.* **108**, 1–5.
Trambly de Laissardière, G. (2003). *Phys. Rev. B*, **68**, 045117.
Trambly de Laissardière, G. (2009). *Z. Kristallogr. New Cryst. Struct.* **224**, 123–126.
Trambly de Laissardière, G. & Fujiwara, T. (1994). *Phys. Rev. B*, **50**, 5999–6005.
Trambly de Laissardière, G., Julien, J.-P. & Mayou, D. (2006). *Phys. Rev. Lett.* **97**, 026601.
Trambly de Laissardière, G. & Mayou, D. (1997). *Phys. Rev. B*, **55**, 2890–2893.
Trambly de Laissardière, G., Nguyen-Manh, D. & Mayou, D. (2005). *Prog. Mater. Sci.* **50**, 679–788.
Trambly de Laissardière, G., Roche, S. & Mayou, D. (1997). *Mater. Sci. Eng. A*, **226–228**, 986–989.
Unal, B., Jenks, C. J. & Thiel, P. A. (2009). *J. Phys. Condens. Matter*, **21**, 055009.
Wencka, M., Vrtnik, S., Koželj, P., Jagličić, Z., Gille, P. & Dolinšek, J. (2017). *Z. Kristallogr. Cryst. Mater.* **232**, 647–652.
Widmer, R., Gröning, O., Ruffieux, P. & Gröning, P. (2006). *Philos. Mag.* **86**, 781–787.
Zijlstra, E. S. & Bose, S. K. (2003). *Phys. Rev. B*, **67**, 224204.
Zijlstra, E. S. & Janssen, T. (2000). *Europhys. Lett.* **52**, 578–583.